

# Template Mode Hierarchies for Binary Black Hole Mergers

James Healy,<sup>1</sup> Pablo Laguna,<sup>1</sup> Larne Pekowsky,<sup>1</sup> and Deirdre Shoemaker<sup>1</sup>

<sup>1</sup>*Center for Relativistic Astrophysics and School of Physics  
Georgia Institute of Technology, Atlanta, GA 30332*

Matched filtering is a popular data analysis framework used to search for gravitational wave signals emitted by compact object binaries. The templates used in matched filtering searches are constructed predominantly from the quadrupolar mode because this mode is the energetically most dominant channel. However, for highly precessing binaries or binaries with moderately large mass ratios, significant power is also carried by higher-order modes. We investigate how the inclusion of higher modes in the templates increases the prospects for detecting gravitational waves. Specifically, we use numerical relativity waveforms from the late inspiral and coalescence of binary black holes to identify mode hierarchies that cover the sky of binary orientations. We show that the ordering in these hierarchies depends on the characteristics of the binary system and the mode strengths. Our study demonstrates that detecting moderately high precessing or unequal mass binaries requires the inclusion of higher modes in the templates banks.

PACS numbers:

## I. INTRODUCTION

Binary systems with black hole (BH) components will provide us with one of the strongest sources of gravitational waves (GWs) soon to be detected by ground-based interferometers [1]. GW observations are accompanied by dazzling engineering, theoretical, and data analysis challenges. One challenge that requires the close cooperation between source model and data analysis researchers is digging out the GW signals from the noisy data. For compact object binaries involving neutron stars and BHs, one of the most popular frameworks to analyze the data is *matched filtering*, which in the broad sense consists of correlating a known signal or *template* with the data in hopes of identifying the presence of the template in the data. Not surprisingly, the success of matched filtering depends mainly on the “quality” of the template, in other words, the degree to which the template captures the correct physics and matches the characteristics of the source. Even with the belief that we possess the correct theory of gravity, Einstein’s theory of general relativity, constructing templates is a laborious and arduous task. A family of binary black hole (BBH) templates needs to sample a 15-dimensional parameter space (BH masses and spins, binary eccentricity, orientation vector, sky position and distance). Furthermore, if the binary merges in the sweet spot of the detector, building templates requires numerical relativity (NR) simulations that capture dynamically strong gravity, thus increasing the computational cost per template significantly.

Without accounting for effects from the orientation of the source, the gravitational radiation from a binary system is dominated by its quadrupolar (2,2) mode component. It should not be surprising then that current data analysis pipelines are predominantly using this mode as a template. An example of the dominance of the (2,2) mode is depicted in Figure 1, where we show the strain amplitude ratio of higher modes relative to the (2,2) mode. The top panel shows the case of an equal mass

BBH and the bottom one with a 1:4 mass ratio. It is evident in both cases the dominance of the (2,2) mode. However, for the unequal mass case, the second strongest mode, the (3,3) mode, is more than 10% of the (2,2), reaching above 20% near merger. On the other hand, for the equal mass case, the second strongest mode is the (4,4) mode, and it is only a few percent of the (2,2) in strength. Similar situations occur for precessing (i.e. spinning BHs) binaries.

If source orientation effects are considered, the relative strength of modes can also be significantly modified. Recently, we carried out a study that addresses such effects for quadrupolar templates [2]. We found that for precessing binaries, overlaps could drop below 0.97 for up to 65% of the sky at the source location. The present study takes the next step. We investigate overcoming the limitations of quadrupolar templates by identify hierarchies of higher modes that could be added to the templates, increasing their sky coverage. Our study assumes that the detector is *optimally oriented*, and we focus on line-of-sight, source orientation effects. Therefore, “the sky” coverages reported will be from a source-centric frame of reference. Furthermore, we focus on BBHs with total mass  $M = 100M_{\odot}$ . For these relatively massive binary systems, interferometers such as LIGO only “see” the late inspiral and merger of the binary. Therefore, templates in this study are obtained entirely from NR simulations. For less massive binaries, the early inspiral becomes more important. The templates in those cases would have to be obtained from hybrid waveforms that stitch NR and post-Newtonian strains [3, 4].

Our study finds that template banks for GW detection based only on the (2,2) mode are probably sufficient for comparable mass, low precession BBHs. At the same time, our work demonstrates that the effectiveness of match filtering is severely impaired for highly precessing or moderately large unequal mass BH systems if templates banks are based entirely on the quadrupolar mode.

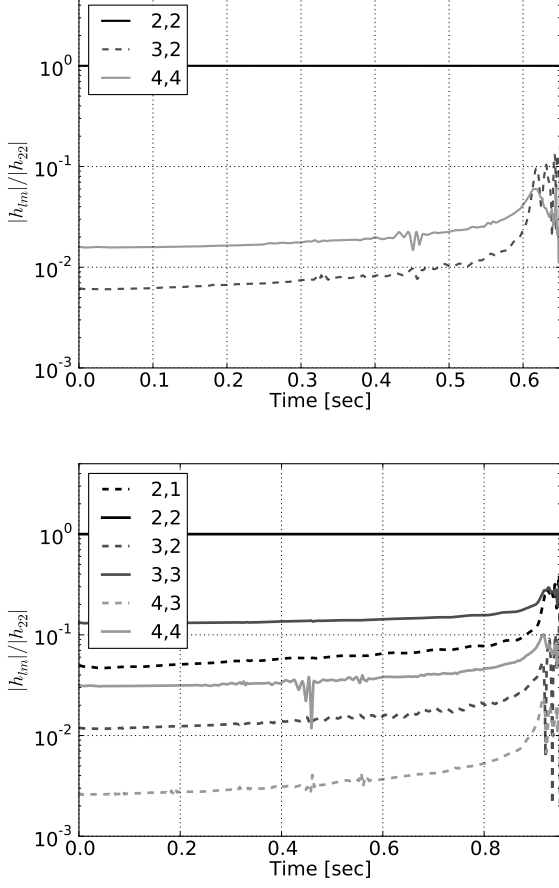


FIG. 1: Strain mode amplitude ratios relative to the (2,2) mode non-spinning BBHs. Top panel shows the case of an equal mass binary, and the bottom panel that of a 1:4 mass ratio system. Modes not included have relative amplitudes less than  $10^{-3}$ .

## II. MATCHED FILTERING AND DETECTION REACH

A GW signal  $s$  impinging an interferometer has the following structure

$$s(t; \bar{\theta}, \bar{\phi}, \psi, \vec{\xi}) = F_+(\bar{\theta}, \bar{\phi}, \psi) h_+(t; \vec{\xi}) + F_\times(\bar{\theta}, \bar{\phi}, \psi) h_\times(t; \vec{\xi}), \quad (1)$$

where  $h_+$  and  $h_\times$  denote the two polarization strains of general relativity.  $h_+$  and  $h_\times$  depend on a parameter vector  $\vec{\xi}$ . Some of the components in  $\vec{\xi}$  are parameters intrinsic to the system, such as the binary eccentricity, BH masses and spins; others are external parameters like the binary orientation and its distance to the detector. In addition, the signal  $s$  depends on the characteristics of the detector through the response or *antenna pattern* functions  $F_+$  and  $F_\times$  [5]. For an interferometer with arms

oriented along the  $x$  and  $y$  axes, these functions read

$$F_+ = -\frac{1}{2}(1 + \cos^2 \bar{\theta}) \cos 2\bar{\phi} \cos 2\psi - \cos \bar{\theta} \sin 2\bar{\phi} \sin 2\psi \quad (2)$$

$$F_\times = \frac{1}{2}(1 + \cos^2 \bar{\theta}) \cos 2\bar{\phi} \sin 2\psi - \cos \bar{\theta} \sin 2\bar{\phi} \cos 2\psi, \quad (3)$$

where the angles  $(\bar{\theta}, \bar{\phi})$  are the location of the binary system in the sky of the detector and  $\psi$  the polarization angle. A detector is optimally oriented if a signal arrives with  $\bar{\theta} = 0$  or  $\pi$  and  $\bar{\phi} = 0$ . On the other hand, the detector is blind for signals with  $\bar{\theta} = \pi/2$ , arriving from directions aligned with the arms of the interferometer. With a network of interferometers, the issue of detector blindness can be alleviated [6, 7]. For this reason, our focus will be on “intrinsic” source orientation effects, which depend only on the direction of propagation of the GW. That is, the signals arriving at the detector will be

$$s(t; \theta, \phi, r, \vec{\xi}_b) = h_+(t; \theta, \phi, r, \vec{\xi}_b) \cos 2\psi + h_\times(t; \theta, \phi, r, \vec{\xi}_b) \sin 2\psi. \quad (4)$$

In Eq. (4), the angles  $(\theta, \phi)$  give the direction of propagation of the GW pointing to the detector from a reference system located at the source,  $r$  is the distance between the source and the detector, and the vector  $\vec{\xi}_b$  denote the parameters intrinsic to the binary (spins, masses and eccentricity). For the present study, the reference system used at the source is the one used to carry out the NR simulations. That is, the reference system has its origin at the center of mass of the binary, and has its  $z$ -axis aligned with the orbital angular momentum at the start of the simulation.

Given the Fourier transforms  $\tilde{A}$  and  $\tilde{B}$  of two real time-dependent signals or waveforms, the inner product with respect to the noise spectrum density  $S_n(f)$  of the detector is given by

$$\langle A|B \rangle = 4 \operatorname{Re} \int_0^\infty df \frac{\tilde{A}(f) \tilde{B}^*(f)}{S_n(f)}. \quad (5)$$

With this inner product, the signal-to-noise (SNR) of a signal  $s$  and a template  $u$  is given by [8]

$$\rho(s, u) = \max_{t_0, \psi_0} \frac{\langle s|u \rangle}{\sqrt{\langle u|u \rangle}}. \quad (6)$$

The maximization over  $t_0$  enters because the signal arrives at an unknown time. Thus, one needs to “slide” the template relative to the signal, which in Fourier space implies replacing  $\tilde{u}(f)$  by  $\tilde{u}(f) \exp(-2\pi i f t_0)$  in Eq. (6). In principle, there is also an unknown phase difference  $\psi_0$  between the signal and the template related to the polarization angle  $\psi$ . This introduces an additional factor of  $\exp(2\pi i \psi_0)$ . If  $u = s$  in Eq (6), one gets the so-called *optimal* SNR  $\rho(s, s) = \sqrt{\langle s|s \rangle}$ .

The *match* or *overlap*  $\mu$  between the signal  $s$  and a template  $u$  is given by

$$\mu(s, u) = \max_{t_0, \psi_0} \frac{\langle s|u \rangle}{\sqrt{\langle s|s \rangle \langle u|u \rangle}}. \quad (7)$$

Thus,  $\rho(s, u) = \mu(s, u) \sqrt{\langle s|s \rangle} = \mu(s, u) \rho(s, s)$ . In some instances, it is more convenient to work with *mismatches*, which are defined as  $\epsilon \equiv 1 - \mu$ . Notice that the  $1/r$  scaling of the signal  $s$  implies that  $\rho \propto 1/r$ . However, because of the normalization factors,  $\mu$  and  $\epsilon$  are independent of  $r$ . Furthermore, the distance scale  $r$  used to construct a template does not play any role because of the normalization factor  $\sqrt{\langle u|u \rangle}$  in Eqs. (6) and (7).

Consider two signals  $s_1$  and  $s_2$  from two identical GW sources,  $s_1$  located at distances  $r_1$  and  $s_2$  at  $r_2$ . Then,

$$\frac{\rho(s_1, u)}{\rho(s_2, u)} = \frac{\mu(s_1, u) \rho(s_1, s_1)}{\mu(s_2, u) \rho(s_2, s_2)} = \frac{\rho(s_1, s_1)}{\rho(s_2, s_2)}, \quad (8)$$

where the last equality follows because the sources are identical, and thus  $\mu(s_1, u) = \mu(s_2, u)$ . On the other hand,

$$\begin{aligned} \rho(s_2, s_2) &= \frac{1}{r_2} \rho(r_2 s_2, r_2 s_2) \\ &= \frac{1}{r_2} \rho(r_1 s_1, r_1 s_1) = \frac{r_1}{r_2} \rho(s_1, s_1), \end{aligned} \quad (9)$$

where we have used that the optimal SNR of a signal times its distance,  $r s$ , is independent of  $r$ . Therefore, we can rewrite Eq. (8) as

$$\frac{\rho(s_1, u)}{\rho(s_2, u)} = \frac{\rho(s_1, s_1)}{\rho(s_2, s_2)} = \frac{r_2}{r_1}. \quad (10)$$

It is wrong to conclude from Eq. (10) that the ratio  $r_2/r_1$  depends on the template  $u$  because of  $\rho(s_1, u)/\rho(s_2, u)$ . The dependence on  $u$  is eliminated because we are considering the same source, just located at different distances.

The SNR property (9) allow one to define for a signal  $s$  a *horizon* distance  $R(s)$  as follows:

$$R(s) = \frac{\rho(\hat{s}, \hat{s})}{\rho(s, s)} \quad (11)$$

where  $\rho(\hat{s}, \hat{s})$  is the optimal SNR of the “signal”  $\hat{s} \equiv r s$ .  $R(s)$  should be interpreted as providing the maximum distance that an interferometer is able to detect a signal  $s$  given an optimal SNR threshold. For instance, during LIGO’s science run S6, the horizon distance of a compact binary coalescence with optimal SNR threshold of  $\rho(s, s) = 8 \text{ Mpc}^{-1}$  was estimated to be  $R(s) \approx 40 \text{ Mpc}$  using as a model for the signal a post-Newtonian strain in the stationary phase approximation [9]. Therefore from Eq. (11),  $\rho(\hat{s}, \hat{s}) \approx 320$ .

For the present study, we are interested in investigating the effect that the choice of a template  $u$  has on the ability of an interferometer to detect a signal  $s$ . Therefore,

instead of the *horizon* distance  $R(s)$ , which is independent of the template, we need a *template reach* distance  $\mathcal{R}(s, u)$ . Since the mismatch  $\mu$  characterizes the “proximity” of a template to a signal, we define the template reach distance as

$$\mathcal{R}(s, u) = \mu(s, u) R(s). \quad (12)$$

Given that  $\mu(s, u) = \mu(\hat{s}, u)$ , we can rewrite Eq. (12) in a form similar to that of Eq. (11):

$$\mathcal{R}(s, u) = \frac{\rho(\hat{s}, u)}{\rho(s, s)}. \quad (13)$$

Notice that  $\mathcal{R}(s, s) = R(s)$  if  $u = s$ ; otherwise,  $\mathcal{R}(s, u) < R(s)$ . Furthermore, the relative change in reach is given by the mismatch:

$$\frac{\delta R}{R} = \frac{R(s) - \mathcal{R}(s, u)}{R(s)} = 1 - \mu(s, u) = \epsilon(s, u). \quad (14)$$

### III. BINARY BLACK HOLE WAVEFORMS

As mentioned in the introduction, the BBHs we consider have total mass  $M = 100 M_\odot$ . For these binaries, interferometers such as advanced LIGO are most sensitive to GW frequencies emitted by the binary during the late inspiral and merger; and, therefore, the templates and signals needed in our study are those constructed entirely from NR simulations. The simulations were produced with the *Maya* code [10–15] of the NR group at Georgia Tech. *Maya* uses the *Einstein Toolkit* [16] which is based on the *CACTUS* [17] infrastructure and *CARPET* [18] mesh refinement. Evolution thorns were generated with the *Kranc* [19] code generator.

We considered a variety of BBH configurations in quasi-circular orbits. Table I gives the characteristics of each binary: BH mass ratio  $q = m_1/m_2$ , dimensionless spin parameters  $\chi$ , angle  $\zeta$  between the BH spin and the  $z$ -axis in the  $xz$ -plane, initial separations  $d/M$ , and grid spacing  $\Delta/M$  in the finest refinement level, and the covering factors  $\tau_{2,2}$  when only the (2,2) mode is used as the template and  $\tau_{2,*}$  which includes all the  $|m| \leq \ell = 2$  modes in the template (see next section). The configurations are classified into three series. Series Q consists of BBH with non-spinning BHs. For the series S, at least one of the BHs is spinning and aligned with the orbital angular momentum; thus, there is no precession. Finally, the series P consists of precessing binary systems.

The templates and signals were built from strains  $h_+$  and  $h_\times$  obtained from the Weyl Scalar  $\Psi_4$ , one of the outputs of the simulations. Specifically, we decompose the Weyl Scalar  $\Psi_4$  produced during the simulation into spin-weighted spherical harmonics as

$$r M \Psi_4(t; \theta, \phi) = \sum_{\ell, m} C_{\ell m}(t) {}_{-2}Y_{\ell m}(\theta, \phi), \quad (15)$$

ID	$q$	$\chi_1$	$\chi_2$	$\zeta_1$	$\zeta_2$	$d/M$	$M/\Delta$	$\tau_{2,2}$	$\tau_{2,*}$
Q01	1.0	0.0	0.0	0	0	11	200	1.000	1.000
Q02	1.5	0.0	0.0	0	0	11	200	1.000	1.000
Q03	2.0	0.0	0.0	0	0	11	200	0.634	0.934
Q04	2.5	0.0	0.0	0	0	11	200	0.356	0.440
Q05	3.0	0.0	0.0	0	0	11	200	0.258	0.299
Q06	4.0	0.0	0.0	0	0	10	240	0.177	0.197
Q07	5.0	0.0	0.0	0	0	10	240	0.144	0.158
Q08	6.0	0.0	0.0	0	0	10	280	0.123	0.134
Q09	7.0	0.0	0.0	0	0	10	320	0.111	0.119
Q10	10.0	0.0	0.0	0	0	8.4	400	0.097	0.103
S01	1.5	0.2	0.2	0	0	11	200	1.000	1.000
S02	1.5	0.4	0.4	0	0	11	200	1.000	1.000
S03	4.0	0.2	0.0	0	0	10	240	0.183	0.198
S04	4.0	0.4	0.0	0	0	10	240	0.191	0.200
S05	4.0	0.6	0.0	0	0	10	240	0.196	0.201
S06	5.0	0.2	0.0	0	0	10	240	0.149	0.160
S07	5.0	0.4	0.0	0	0	10	240	0.154	0.161
S08	5.0	0.6	0.0	0	0	10	240	0.160	0.164
S09	6.0	0.2	0.0	0	0	10	280	0.127	0.136
S10	6.0	0.4	0.0	0	0	10	280	0.134	0.139
S11	6.0	0.6	0.0	0	0	10	280	0.139	0.142
P01	1.5	0.6	0.6	45	0	10	120	1.000	1.000
P02	1.5	0.6	0.6	60	0	10	120	1.000	1.000
P03	1.5	0.6	0.6	90	0	10	120	0.779	1.000
P04	2.0	0.6	0.6	45	0	10	120	0.554	0.982
P05	2.0	0.6	0.6	60	0	10	120	0.375	0.981
P06	2.0	0.6	0.6	90	0	10	120	0.222	0.933
P07	2.0	0.6	0.6	135	0	10	120	0.370	0.963
P08	2.0	0.6	0.6	270	0	10	120	0.327	0.933
P09	2.5	0.4	0.4	45	0	10	120	0.312	0.451
P10	2.5	0.4	0.4	60	0	10	120	0.291	0.456
P11	2.5	0.4	0.4	90	0	10	120	0.208	0.471
P12	2.5	0.6	0.6	45	0	10	120	0.258	0.465
P13	2.5	0.6	0.6	60	0	10	120	0.213	0.485
P14	2.5	0.6	0.6	90	0	10	120	0.162	0.510
P15	4.0	0.6	0.6	45	0	10	120	0.099	0.218
P16	4.0	0.6	0.6	60	0	10	120	0.057	0.224
P17	4.0	0.6	0.6	90	0	10	120	0.019	0.247
P18	4.0	0.6	0.6	0	270	10	140	0.193	0.204
P19	4.0	0.6	0.6	90	270	10	140	0.001	0.242
P20	4.0	0.6	0.6	150	270	10	140	0.155	0.225
P21	4.0	0.6	0.6	180	270	10	140	0.188	0.234
P22	4.0	0.6	0.6	210	270	10	140	0.130	0.218
P23	4.0	0.6	0.6	270	270	10	140	0.026	0.244

TABLE I: Characteristics of the BBH systems used in this study.  $q = m_1/m_2$  denotes the BH mass ratio,  $\chi_{1,2}$  the dimensionless spin parameter,  $\zeta_{1,2}$  the angle between the BH spin and the  $z$ -axis in the  $xz$ -plane,  $d/M$  the initial binary separation, and  $\Delta/M$  the grid spacing at the finest mesh. The last two columns give the covering factor  $\tau_{2,2}$  when only the (2,2) mode is used as the template and the covering factor  $\tau_{2,*}$  when the template includes all the  $|m| \leq \ell = 2$  modes.

where the angles  $\theta$  and  $\phi$  are relative to a coordinate system with origin at the center-of-mass of the binary and with a  $z$ -axis aligned with its orbital angular momentum at the beginning of the simulation. Then, we solve  $\Psi_4 = \ddot{h}_+ - i \ddot{h}_\times = \ddot{h}^*$  to get the strains

$$\frac{r}{M} h(t; \theta, \phi) = \sum_{\ell, m} H_{\ell m}(t) {}_{-2}Y_{\ell m}^*(\theta, \phi) \quad (16)$$

For our signals  $s$ , we calculate  $h_+$  containing all the  $(\ell, m)$  modes with  $2 \leq \ell \leq 5$ . The templates  $u$  are constructed from different subsets among all the 32  $(\ell, m)$  modes for the signals. Explicitly, a template  $u_n$  containing  $n \leq 32$  modes is given by

$$u_n = \sum_{i=1}^n w_i \quad (17)$$

with  $w_i$  denoting a mode in the sense of Eqs. (16), i.e.,  $w_i = H_{\ell m}(t) {}_{-2}Y_{\ell m}^*(\theta, \phi) M/r$  in which the index  $i$  collectively labels  $(\ell, m)$ . To avoid the integration to strain, and the errors associated with it, we calculate the strain in the frequency domain for the matches, that is,  $\tilde{h} = \tilde{\Psi}_4^*/(-4\pi^2 f^2)$ .

#### IV. COVERING FACTORS AND MODE HIERARCHIES

As mentioned in Sec. II, the focus of our analysis is the mismatch  $\epsilon$  of a signal  $s(\vec{\xi}_s)$  with a template  $u(\vec{\xi}_u)$ , where the parameter vectors  $\vec{\xi}_s$  and  $\vec{\xi}_u$  include both, intrinsic physical (BH masses and spins) and extrinsic (position of the source in the sky of the detector and orientation of the binary) parameters. Since we are only concerned with line-of-sight orientation effects, we will assume that the detector is *optimally oriented* and  $\vec{\xi}_s = \vec{\xi}_u$ , and in particular  $(\theta_s, \phi_s) = (\theta_u, \phi_u)$ . As a consequence, once a source is selected,  $\epsilon$  will only depend on the location of the source in the sky, i.e.  $\epsilon = \epsilon(\theta, \phi)$  as implied by Eq. (4).

We will mostly present results as sky-maps, and investigate how  $\epsilon(\theta, \phi)$  depends on the particular content of higher modes in the template. We construct sky-maps with  $61 \times 61$  pixels; each pixel “colored” with its value of  $\epsilon$ . Figure 2 gives an example of two sky-maps of mismatches for a BBH with mass ratio  $q = 4$ . The top panel shows a non-precessing binary (case Q06 in Table I) in which the template contains only the (2,2) mode. The bottom panel shows a precessing binary (case P19 in Table I). The template in this case contains all the  $m$ -modes for  $\ell = 2$ . Notice that, the mismatch is smaller around the poles in the non-precessing case. On the other hand, for the precessing case, the region where the mismatches are smaller have been shifted due to the precession of the system.

In addition to the sky-maps, given a mismatch tolerance  $\epsilon_{\text{mx}}$ , we label a pixel *on* if  $\epsilon < \epsilon_{\text{mx}}$  and *off* otherwise. With the on-pixels, we estimate the covering factor

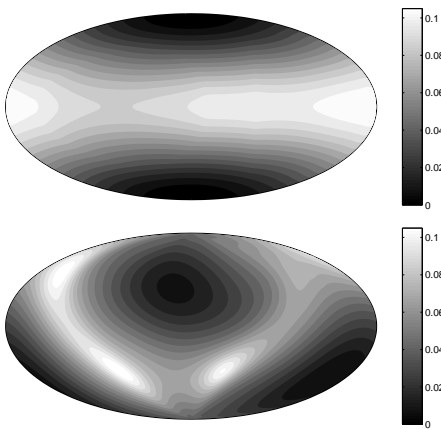


FIG. 2: Representative sky-maps of mismatches for a BBH with mass ratio  $q = m_1/m_2 = 4$ . The top panel shows a non-precessing binary (case Q06) in which the template contains only the (2,2) mode. In the bottom panel, the precessing case P19 is shown using a template that contains all the  $m$ -modes for  $\ell = 2$ .

$\tau(\epsilon_{\text{mx}})$  of a template as the fraction of the sky where  $\epsilon < \epsilon_{\text{mx}}$ . This means that a template that cannot detect any signals would have a covering factor of 0, and a template that matches all signals would have a covering factor of 1. From now on, when stating covering factors, we will just use  $\tau$ , understanding that  $\epsilon_{\text{mx}}$  is implied. Unless explicitly specified, we use  $\epsilon_{\text{mx}} = 0.03$  in the remainder of the paper, a customary value within the GW data analysis community. For instance, the covering factors for the cases in Figure 2 are  $\tau = 0.177$  (top) and  $\tau = 0.242$  (bottom).

It should not be surprising that the mode content in a template has an impact on its mismatch with the signal, and thus its covering factor. Our goal is then to find the optimal template  $u_N$  that yields a target covering factor  $\tau_{\text{tg}}$ . We use a *greedy* algorithm for this purpose. The end result is a sequence of templates  $\{u_n\}$  built from a set of modes  $\{w_n\}$  as in Eq. (17), with  $n = 1 \dots N$ . At each step in the sequence, a template  $u_n$  is locally optimal in its ability for improving sky coverage and reaching  $\tau_{\text{tg}}$ . Furthermore, the template sequence is ordered in a *hierarchy* with respect to their sky coverage capabilities. The procedure we use to obtain this hierarchy involves three stages.

*First Stage:* The first template  $u_1$  is selected to be the dominant (2,2) mode. The covering factor for this first template is denoted by  $\tau_1$ . The second template  $u_2$  is obtained from a superposition of the previous template,  $u_1$ , and a mode  $w_i$  selected from the remaining 31 modes. This yields 31 potential candidates for  $u_2$ . We promote to template  $u_2$  the candidate that delivers the best improvement in sky coverage over the value  $\tau_1$ . The third template in the hierarchy is constructed in a similar fashion. That is,  $u_3 = u_2$  plus one of the 30 remaining  $w_i$  modes. Among the 30 candidates for  $u_3$ , we keep the one with the largest improvement in sky coverage over

the value  $\tau_2$ . This process is repeated until we obtain a template,  $u_N$ , such that  $\tau_N \geq \tau_{\text{tg}}$ .

*Second Stage:* Because the procedure to get  $\{u_n\}$  is locally optimal, it is not guaranteed that the sequence has the minimum possible number of steps to reach  $\tau_{\text{tg}}$ , in other words, that the template  $u_N$  has the minimum number of modes. Next is to identify all modes in  $u_N$  that could be excluded and still have  $\tau_N \geq \tau_{\text{tg}}$ . Starting with  $u_N$ , we construct templates

$$u_n^* = u_N - w_n = \sum_{i=1}^N w_i - w_n = \sum_{i \neq n}^N w_i \quad (18)$$

for  $n = 1 \dots N$ . We then select the  $u_n^*$  for which  $\tau_n^* \geq \tau_{\text{tg}}$ . If there is more than one template  $u_n^*$ , we single out the case in which the highest mode was subtracted. That mode is then removed from the template  $u_N$  and set  $\bar{u}_{N-1} = u_n^*$ , which contains  $N - 1$  modes. The same process is applied now to  $\bar{u}_{N-1}$ . That is, we construct templates

$$u_n^* = \bar{u}_{N-1} - w_n = \sum_{i=1}^{N-1} w_i - w_n = \sum_{i \neq n}^{N-1} w_i \quad (19)$$

for  $n = 1 \dots N - 1$ . The outcome is a new template  $\bar{u}_{N-2}$ . The process is repeated  $L$  times until we are not able to construct templates  $u_n^*$  such that  $\tau_n^* \geq \tau_{\text{tg}}$ . The resulting  $\bar{u}_M$ , with  $M = N - L$ , is the template with the minimum number of modes having a covering factor  $\tau_{\text{tg}}$ .

*Third Stage:* With the template  $\bar{u}_M$  at hand, we apply a greedy algorithm to re-construct the hierarchy but now in reverse order; that is, starting with  $\bar{u}_M$  we obtain  $\bar{u}_{M-1}$  as the template that decreases  $\bar{\tau}_M$  the least. We continue until we reach a template made out of a single mode.

Tables II, III and IV show how our greedy algorithm builds a hierarchy for the P17, P19 and P20 cases, respectively. The top row labels the  $(\ell, m)$  modes, and the left column denotes the covering factor  $\tau$ . The target covering factor is  $\tau_{\text{tg}} = 1$ . For a given  $\tau$ , the Xs in the row indicated the modes that were included in the template. The Os denote the mode from the previous step that was removed. The first horizontal line denotes the end of the *first stage* in the greedy algorithm. The rows between the first and second line are the steps involved in the *second stage*. Finally, below the second line are the templates in hierarchy one is seeking, in decreasing order of sky coverage.

## V. RESULTS

A sense of the effectiveness of the mode (2,2) in covering the sky is given in the second to last column of Table I where we report the covering factor of just the (2,2) mode, given by  $\tau_{2,2}$ . As long as  $q \leq 1.5$ , the (2,2) mode will effectively cover the entire sky for non-spinning

[illegible]



$\tau \backslash l, m$	2	3	4	5	5	5	5	5	5	2	3	2	3	2	2
	2	3	4	5	4	3	2	1	0	0	1	-2	-3	-1	1
0.155	X														
0.506	X	X													
0.588	X	X	X												
0.597	X	X	X	X											
0.591	X	X	X	X	X										
0.573	X	X	X	X	X	X									
0.548	X	X	X	X	X	X	X								
0.542	X	X	X	X	X	X	X	X							
0.535	X	X	X	X	X	X	X	X	X						
0.534	X	X	X	X	X	X	X	X	X	X					
0.555	X	X	X	X	X	X	X	X	X	X	X				
0.563	X	X	X	X	X	X	X	X	X	X	X	X			
0.747	X	X	X	X	X	X	X	X	X	X	X	X	X		
0.950	X	X	X	X	X	X	X	X	X	X	X	X	X	X	
1.000	X	X	X	X	X	X	X	X	X	X	X	X	X	X	X
1.000	X	X	X	O	X	X	X	X	X	X	X	X	X	X	X
1.000	X	X	X		O	X	X	X	X	X	X	X	X	X	X
1.000	X	X	X			O	X	X	X	X	X	X	X	X	X
1.000	X	X	X				O	X	X	X	X	X	X	X	X
1.000	X	X	X					O	X	X	X	X	X	X	X
1.000	X	X	X						O	X	X	X	X	X	X
1.000	X	X	O							X	X	X	X	X	X
1.000	X	X								X	O	X	X	X	X
0.957	X	X								O		X	X	X	X
0.748	X	X										X	X	X	O
0.565	X	X										X	X	O	
0.406	X	X										X	O		
0.506	X	X										O			
0.155	X	O													

TABLE IV: **P20 Hierarchy**: Same as in Table II but for the P20 case.

precessing cases, by a significant amount more.

#### A. Q-series

We first analyze the impact of adding other modes to the quadrupolar templates for the Q-series. To anticipate what to expect from the greedy algorithm described in Sec. IV, we will consider first adding modes based only on their energy radiated; these are (3,3), (4,4) and (2,1) for the Q-series. Adding the (3,3) mode translates into a significant improvement as depicted in the top panel in Figure 3 where we show a bar chart of the covering factor as a function of the mass ratio. For each bar, black denotes the covering factor that is achieved with only the (2,2) mode. The gray bar above black is the enhancement that one gets by considering a template with (2,2) + (3,3). One sees that now full coverage is obtained for  $q \leq 3$  and substantial coverage improvement of  $0.5 \leq \tau \leq 0.75$  for  $7 \geq q \geq 5$ , and  $\tau = 0.45$  for  $q = 10$ . Adding

the next most energetic mode, the (4,4) mode, produces coverage above 0.8 for the remaining cases except  $q = 10$ , as seen by the white bars in Figure 3 top panel. Full coverage for all the mass ratios considered is achieved when the (2,1) is added (light gray bars).

The ordering based on energetic used for the Q-series gets slightly modified if one uses our greedy algorithm. The method reveals that adding the (2,1) mode before the (4,4) mode is more optimal in reaching full coverage, as seen in the bottom panel of Figure 3. The reason why the greedy algorithm favors the (2,1) mode for  $q > 4$  is because, although the mode is less energetic, it channels energy into regions of the sky not covered by the (2,2)+(3,3) template more effectively than the (4,4) mode. This can be seen in Figure 4 for the  $q = 10$  case in the Q-series. Each of the panels in this figure shows the percentage of total energy emitted in a given direction that is channeled through the modes present in a template. From top to bottom, the panels show the cases for templates (2,2), (2,2)+(3,3), (2,2)+(3,3)+(4,4), and



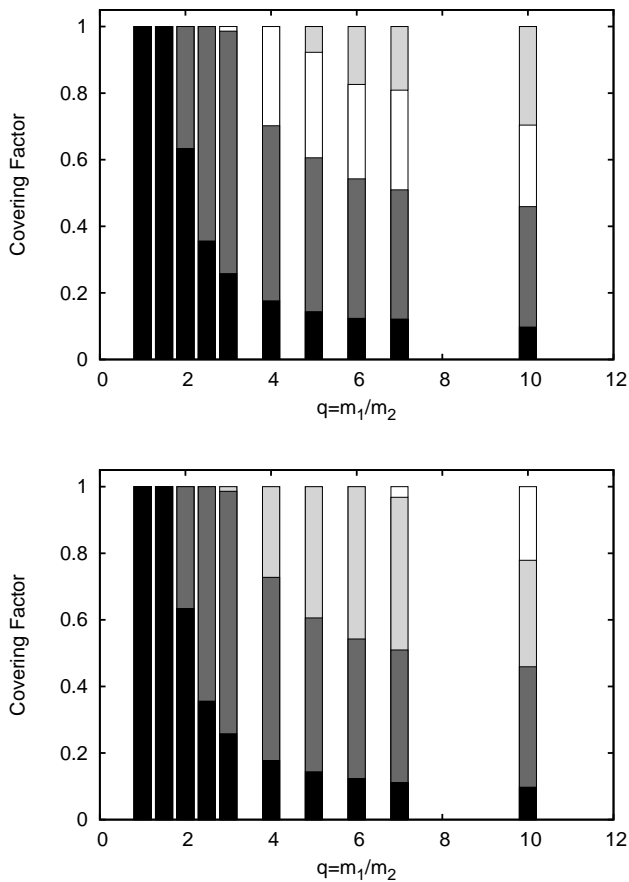


FIG. 3: Covering factors as a function of mass ratio for the Q-series. Each portion of the bar chart represents the contribution to the covering factor by adding a mode. In each bar, bottom to top is the order used in adding modes. The gray scale is as follows: black (2,2) mode, gray (3,3) mode, white (4,4) mode and light gray (2,1) mode. Top panel shows the case in which modes are added according to their energy emission strength. The bottom panel shows the hierarchy order obtained by our greedy algorithm, which translates into reversing the order of the (4,4) and (2,1) modes.

(2,2)+(3,3)+(2,1), respectively. The black lines in each figure denote mismatches  $\epsilon = 0.03$  between the template and the signal. Darker regions have mismatches  $\epsilon > 0.03$ . Thus, not surprisingly, there is a correlation between the amount of energy captured by the template and its mismatch value. Roughly speaking, regions for which the template captures more than 80% of the energy emitted in a given direction have  $\epsilon \leq 0.03$ . In these regions of low mismatch, the average percentage radiated in all four panels of Figure 4 is approximately 90% overall. It is then evident from the bottom two panels in Figure 4, that adding the (2,1) mode before the (4,4) yields a larger region where the template better captures the energy emitted.

We have also found that there is a degree of degeneracy. For instance, in the  $q = 7$  case, adding to the

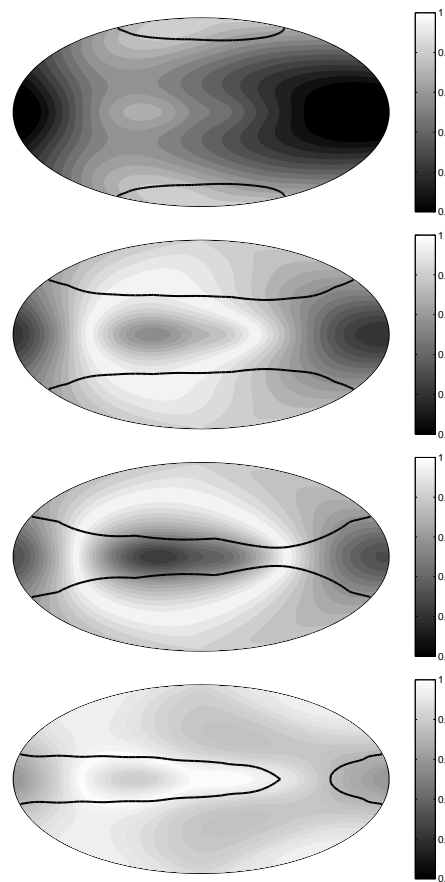


FIG. 4: Percentage of total energy emitted in a given direction that is channeled through the modes present in a template for the  $q = 10$  case in the Q-series. From top to bottom, the panels show the cases for templates (2,2), (2,2)+(3,3), (2,2)+(3,3)+(4,4), and (2,2)+(3,3)+(2,1), respectively. The black lines in each figure denote mismatches  $\epsilon = 0.03$  between the template and the signal. Light regions with values larger than 0.8 have mismatches  $\epsilon < 0.03$ .

template (2,2)+(3,3)+(2,1) the mode (4,4) or the mode (5,5) accomplishes full coverage. That is, both modes contain enough power in comparable parts of the sky.

## B. S-series

Next to analyze is the S-series, consisting of BBHs with spinning BHs aligned with the orbital angular momentum, i.e. non-precessing binaries. As mentioned before, for low mass ratio  $q \leq 1.5$ , the quadrupolar mode is able to get good coverage of the sky. We will focus then on the  $q = 4, 5$  and  $6$  cases in Table I. These are binaries with only one of the BHs spinning. As with Figure 3, the bar charts in Figure 5 show the incremental effectiveness of adding modes to a template. In this case, the covering factor is plotted as a function of the dimensionless spin parameter  $\chi_+$ . The gray scale is: black (2,2) mode, gray (3,3) mode and light gray (2,1) mode. From top

to bottom, the panels show the  $q = 4, 5$  and  $6$  cases, respectively.

The first thing to notice is that if only the (2,2) mode is used as a template, the covering factors (black bars) are basically independent of the spin. In addition, the values of the covering factors for the (2,2) mode template decrease as the mass ratio increases. The big changes occur when one adds the (3,3) mode to the quadrupolar template. In some instances, one is able to increase the coverage to include the entire sky. It is also interesting that the influence of this mode increases with the value of the spin, consistent with the energy of the (2,2) and (3,3) modes increasing with spin. For example, in the  $q = 4$  case, a (2,2)+(3,3) template is able to saturate the sky for  $\chi_+ \geq 0.4$ . Finally, for those cases in which the (3,3) is not able to yield full sky coverage, i.e. low spin, high mass ratio binaries, adding the (2,1) mode completes the sky.

### C. P-series

The last series focused on precessing binaries. In this series, our greedy algorithm used to construct hierarchies provided insights on the number of modes that will be needed for detecting GW from astrophysically realistic binaries. We applied the greedy algorithm to each of the 23 cases in the series. However, we show the steps that the algorithm takes for only the P17, P19 and P20 cases. The steps are shown in Tables II, III and IV, respectively.

A dramatic aspect found for these highly precessing binaries is that it takes a substantial number of modes to cover at least 60% of the sky. For the P17 case, one sees from Table II that one needs a template with 8 modes:  $(2, \pm 2)$ ,  $(2, \pm 1)$ ,  $(2, 0)$ ,  $(3, 3)$ ,  $(3, -2)$  and  $(3, 0)$ . Similarly, for the P19 in Table III, the template contains the  $(2, \pm 2)$ ,  $(2, \pm 1)$ ,  $(2, 0)$ ,  $(3, 3)$  and  $(3, 0)$  modes. Finally, for the P20 case, as seen from Table III, the template involves the  $(2, \pm 2)$  and  $(3, \pm 3)$  modes. The entire hierarchy for each case is listed below the second line in each of the Tables ordered in decreasing covering factor. It is clear then that precession plays a big role on the outcome of the hierarchy, and in particular the modes that are needed for full coverage of the sky (i.e. the row below the second line in the tables).

To quantify the influence of precession, Figure 6 shows the total number of modes needed for full coverage in the P-series organized by mass ratio value  $q$  and spin  $\chi$ . The number of modes are given as a function of the angle  $\Theta$  where  $\cos \Theta = (\vec{L} \cdot \vec{S})/(LS)$ . Here  $\vec{L}$  is the orbital angular momentum and  $\vec{S} = \vec{S}_1 + \vec{S}_2$  the total spin at the beginning of the simulations. Between  $0^\circ \leq \Theta \leq 90^\circ$ , the larger the angle  $\Theta$  the higher the observed precession in the system; and, therefore, it is not surprising in this range of angles for Figure 6 to indicate that the number of modes needed for full sky coverage grows monotonically with  $\Theta$ . One can also see that, for a given  $\Theta$  angle value, the number of modes needed also increases monotonically

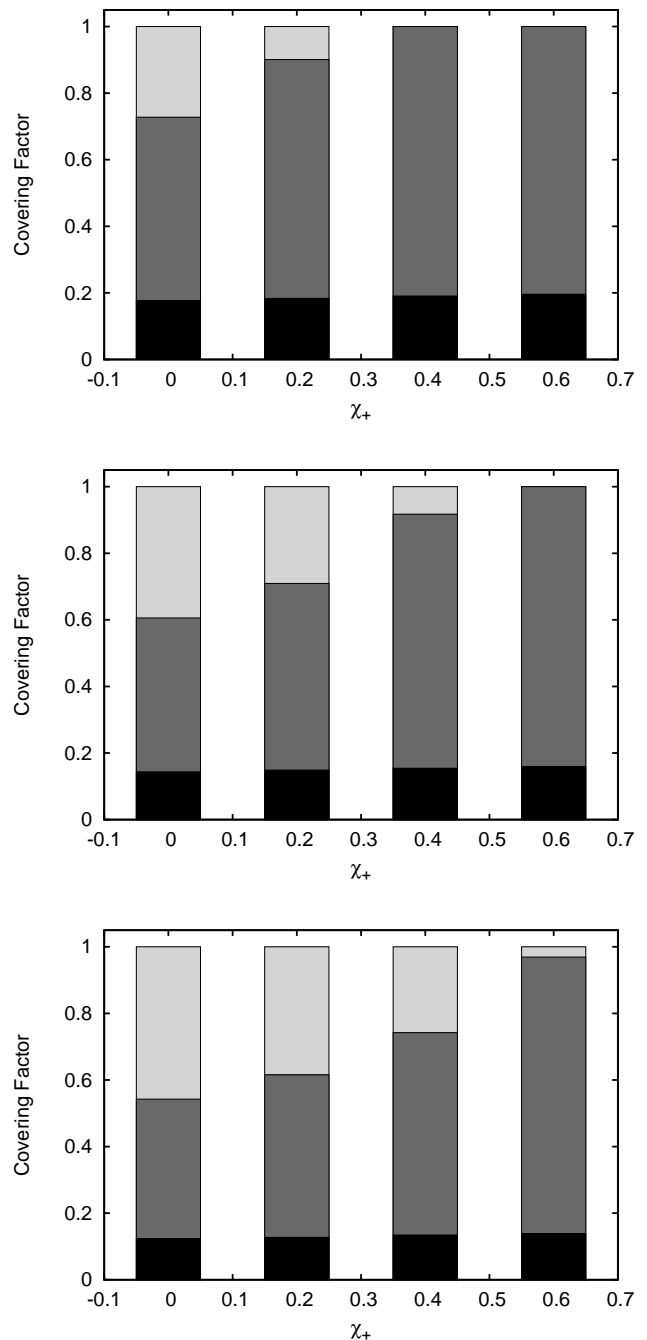


FIG. 5: Covering factors versus spin,  $\chi_+ = a_+/m_+$ , of the more massive BH. The less massive BH has vanishing spin. The top panel is  $q = 4$ , center  $q = 5$ , and bottom  $q = 6$ . The gray scale is as follows: black (2,2) mode, gray (3,3) mode, and light gray (2,1) mode.

with the mass ratio  $q$ . For angles  $\Theta \geq 180^\circ$ , we only have a few data points. But it is clear that the monotonicity no longer applies since for those cases the level of precession decreases.

To check the robustness of our algorithm in finding hierarchies, we selected two  $q = 4$  binaries, one non-

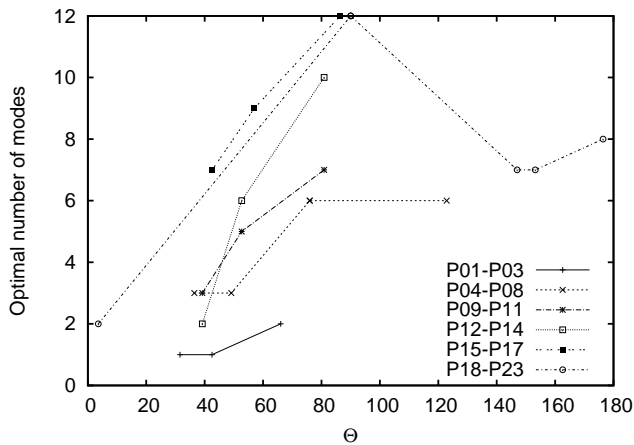


FIG. 6: Optimal number of modes needed for full coverage versus  $\Theta = \arccos(\vec{L} \cdot \vec{S}/(LS))$  for all precessing simulations in the P-series.

precessing (Q06) and the other with one of the highest precession (P23). We ran these two cases at different resolutions:  $(M/160, M/180, M/200)$  for Q06 and  $(M/140, M/160, M/180)$  for P23. In addition, we constructed the GWs from the simulations at three different extraction radii ( $r = 60, 75, 90M$ ). Our greedy algorithm was able to follow identical steps and find the same hierarchy for the Q06 case. For the precessing case P23, there were small differences in the steps taken for the lowest resolution and smallest extraction radii case, but the resulting hierarchy remained the same.

We also experimented with steps that add and remove  $(\ell, |m|)$  and  $(\ell, -|m|)$  modes simultaneously. This reduced the number of total possible steps from 31 to 17 after the initial seed of  $(2, \pm 2)$ . The net effect was to shrink or eliminate Stage 2. We also found that there were very few cases where the resulting hierarchy contained fewer modes than the single mode case.

## VI. CONCLUSIONS

As the NR community explores the complete, generic parameter space of BBH spacetimes, non-dominant modes play an increasingly important role in detecting and characterizing potential gravitational wave signals. In this paper, we introduced a hierarchical, greedy method to identify the modes necessary for full sky coverage. We define sky coverage as the percent of sky in a source-centric frame that a template will match with nature up to a mismatch threshold, here taken as 0.03.

The loss of sky coverage is most noticeable in highly unequal and precessing BBH systems. As long as  $q \leq 1.5$ , the  $(2,2)$  mode will effectively cover the entire sky for spinning and mildly precessing systems. For non-spinning systems, as the mass ratio increases to  $q \geq 7$ , the inclusion of four modes is necessary. In the absence

of precession, a larger spin magnitude increases the energy of the system and fewer modes are necessary. As precession becomes more dramatic, as measured by  $\Theta$ , the range of sky covered decreases to below 60-90% and the number of modes necessary to achieve full coverage increases to 12 for the many of the cases studied here. For non-precessing systems, the four important modes are also the four most energetic:  $(2,2)$ ,  $(3,3)$ ,  $(4,4)$ , and  $(2,1)$ . For all precessing systems covered here, all the  $\ell = 2$  and  $\ell = 3$  modes are sufficient for covering all possible orientations.

Although we have focused on binaries with total mass of  $100 M_\odot$ , our methodology is directly applicable to less massive systems, where templates are constructed from hybrid waveforms that combine post-Newtonian and NR results into one, long waveform. In broad terms, our conclusions regarding the influence of higher modes are likely to carry over to lighter binaries, see for instance Figure 1 and related work in [20], and thus have an important impact for the enterprise of building template models. Our method could potentially give clues where effort in analytic modeling, NR simulations, and hybridization techniques will yield the most benefit. In particular, it should be possible to estimate the loss in sky coverage due to missing information resulting from using a subset of modes.

In current GW data analysis searches based on matched filtering, waveform models are used to construct a bank of templates placed at discrete points in the two-dimensional parameter space spanned by total mass  $M$  and mass ratio  $q$  [21]. Such a bank responds not only to GW signals, but also to noise in the detector, creating a population of false alarm triggers in the search pipelines. As a consequence, a true signal must stand out sufficiently above those triggers in order to be claimed as a detection. If one were to utilize higher-mode information, it would become necessary to increase the dimensionality of the template bank by two to include the orientation parameters  $\theta$  and  $\phi$ . There is a potential tension in doing so. Although the additional templates will assist in responding better to the presence of signals, the increased number of templates will unfortunately also elevate the population of false alarm events thus impairing detection ability. In order to maximize the template response and minimize the emergence of false alarm triggers, one would have to adjust various aspects in the current search methodologies. For example, currently two distinct searches are performed, one covering the mass region  $M \leq 25M_\odot$  and another spanning  $25M_\odot < M \leq 100M_\odot$ . This is done in part because the background populations generated by templates in these two regions differ significantly. It is possible that higher-mode information could best be employed by further subdividing by mass ratio. The NINJA-2 project [22], which is currently ongoing, provides one possible route to investigating such issues. NINJA-2 will be able to add complete hybrid waveforms which include higher modes into realistic next-generation detector noise. Using the

resulting combined data with guidance from techniques such as the one introduced here may be able to help assess the difficulties and rewards of higher-mode templates in a complete search.

## VII. ACKNOWLEDGMENTS:

Work supported by NSF grants 1205864, 1212433, 0903973, 0941417 and 0955825. Computations at

XSEDE TG-PHY120016 and the Cygnus cluster at Georgia Tech.

- 
- [1] M. Pitkin, S. Reid, S. Rowan, and J. Hough, *Living Reviews in Relativity* **14** (2011), URL <http://www.livingreviews.org/lrr-2011-5>.
  - [2] L. Pekowsky, J. Healy, D. Shoemaker, and P. Laguna, *ArXiv e-prints* (2012), 1210.1891.
  - [3] M. Hannam, S. Husa, F. Ohme, and P. Ajith, *Phys.Rev.* **D82**, 124052 (2010), 1008.2961.
  - [4] M. Boyle, *Phys.Rev.* **D84**, 064013 (2011), 1103.5088.
  - [5] W. G. Anderson, P. R. Brady, J. D. E. Creighton, and E. E. Flanagan, *Phys. Rev. D* **63**, 042003 (2001), URL <http://link.aps.org/doi/10.1103/PhysRevD.63.042003>.
  - [6] B. F. Schutz, *Classical and Quantum Gravity* **28**, 125023 (2011), 1102.5421.
  - [7] N. Kanda and the LCGT collaboration, *ArXiv e-prints* (2011), 1112.3092.
  - [8] M. Maggiore, *Gravitational Waves - Volume 1* (Oxford University Press, New York, NY, 2008), 1st ed.
  - [9] The LIGO Scientific Collaboration and The Virgo Collaboration, *ArXiv e-prints* (2012), 1203.2674.
  - [10] R. Haas, R. V. Shcherbakov, T. Bode, and P. Laguna, *Astrophys.J.* **749**, 117 (2012), 1201.4389.
  - [11] J. Healy, T. Bode, R. Haas, E. Pazos, P. Laguna, et al. (2011), 1112.3928.
  - [12] T. Bode, P. Laguna, and R. Matzner, *Phys.Rev.* **D84**, 064044 (2011), 1106.1864.
  - [13] T. Bode, T. Bogdanovic, R. Haas, J. Healy, P. Laguna, et al., *Astrophys.J.* **744**, 45 (2012), 1101.4684.
  - [14] T. Bode, R. Haas, T. Bogdanovic, P. Laguna, and D. Shoemaker, *Astrophys. J.* **715**, 1117 (2010), 0912.0087.
  - [15] J. Healy, J. Levin, and D. Shoemaker, *Phys. Rev. Lett.* **103**, 131101 (2009), 0907.0671.
  - [16] et-web, einstein Toolkit home page:<http://www.einsteintoolkit.org>.
  - [17] cactus-web, cactus Computational Toolkit home page:<http://www.cactuscode.org>.
  - [18] E. Schnetter, S. H. Hawley, and I. Hawke, *Class. Quant. Grav.* **21**, 1465 (2004).
  - [19] S. Husa, I. Hinder, and C. Lechner, *Computer Physics Communications* **174**, 983 (2006).
  - [20] D. A. Brown, P. Kumar, and A. H. Nitz (2012), 1211.6184.
  - [21] S. Babak, R. Biswas, P. Brady, D. Brown, K. Cannon, et al. (2012), 1208.3491.
  - [22] P. Ajith, M. Boyle, D. A. Brown, B. Bruggmann, L. T. Buchman, et al., *Class.Quant.Grav.* **29**, 124001 (2012), 1201.5319.